



Nascent Titanium/Silicon-Containing Particle Formation in Corona Discharge Assisted Combustion

Chanakya Bagya Ramesh¹, Frank Daoru Han², Yang Wang¹

¹Department of Chemical, Environmental, and Materials Engineering, University of Miami, Coral Gables, Florida, 33146, United States

²Department of Mechanical and Aerospace Engineering, Missouri University of Science and Technology, Rolla, Missouri, 65409, United States

Correspondence to: Yang Wang (yangwang@miami.com)

Abstract. Plasma-assisted combustion (PAC) is a technology that introduces high concentrations of charges, ions, and radicals, making the flame more stable and efficient. At the same time, PAC has also been shown to alter particle formation during combustion. Here, we investigate the effect of a high-frequency (~21 kHz) alternating current (AC) corona discharge on particle formation and growth in a premixed flame, especially at the initial stages (with particle sizes below 10 nm). We first examined the mobility size distribution of ions generated from non-plasma combustion and corona discharge-assisted combustion. The mobility size for positive ions does not change with the introduction of plasma. However, the negative ions change towards a larger size, likely due to different ion chemistry from plasma. We then introduced corona discharge with varying powers into the flame that contains titanium isopropoxide (TTIP) or tetraethyl orthosilicate (TEOS) and obtained the size distribution of the synthesized nanoparticles. We found that particle growth is suppressed by the corona discharge under relatively higher precursor feed rates (above ~29 mg h⁻¹ for TTIP and above ~60 mg h⁻¹ for TEOS). The mobility diameter is suppressed by up to 12% for TTIP and by up to 20% for TEOS. We further used different charging models to examine the impact of plasma on particle formation. In the case of higher precursor feed rates, the incipient particle concentration is high within the flame region. As higher number of charges accumulated on particles from negative charge carriers (including electrons and negative ions) than positive ions, the particles are preferentially charged negative. Such preferential charging results in particle-particle repulsion which suppresses coagulation particle growth. The findings of this study can guide nanoparticle synthesis and particulate matter control using PAC.

25 1 Introduction

Nanomaterial production is a significant global industry, valued at approximately \$12.4 billion in 2023 (Nanotechnology and nanomaterials market, 2025). Recent advancements in battery technology, drug delivery systems, and energy conversion have driven a growing demand for nanomaterials, with a projected compound annual growth rate (CAGR) of 15% over the next six years (Nanotechnology and nanomaterials market, 2025). Combustion synthesis is considered one of the most effective methods for producing nanomaterials (Li et al., 2016), and a substantial portion of current nanomaterial production



relies on combustion-based processes. These processes employ aerosol-focused technologies to control and optimize production, leveraging the bottom-up approach at the nanometer scale. Due to the rapid formation of aerosols within the coupled thermal and flow fields in combustion synthesis, the properties of the synthesized nanomaterials are sensitive to flame instability and fuel incomplete combustion, which may deteriorate the quality of the synthesized nanomaterials.

35 One technology proposed to reduce flame instability and promote fuel combustion is plasma-assisted combustion (PAC). PAC introduces plasmas into combustion and studies have shown that this makes the flame more stable (Bradley and Nasser, 1984; Galley et al., 2005; Liao and Zhao, 2018; Vincent-Randonnier et al., 2007) and efficient (Galley et al., 2005; De Giorgi et al., 2017; Rosocha et al., 2004), while also reducing emissions (Cha et al., 2005). These improvements have been observed across various types of non-equilibrium plasmas, including a corona discharge (Bradley and Nasser, 1984),
40 nanosecond repetitive pulse discharge (Galley et al., 2005), dielectric barrier discharge (Cha et al., 2005; De Giorgi et al., 2017; Rosocha et al., 2004), and microwave discharge (Ehn et al., 2017). The benefits have been attributed to the high concentration of charge carriers and radicals generated by the plasma (De Giorgi et al., 2017), which influence both the chemical reactions responsible for forming nascent particles and the growth of these particles during combustion. Since the properties of these charge carriers and radicals can be altered by changing the properties of plasma, PAC provides an
45 opportunity to engineer the synthesis of nanomaterials. Apart from these positive effects, the introduction of electric fields to flames at sub-breakdown voltages may also produce adverse effects. Under such conditions, both DC and AC electric fields have been reported to induce flame instability by displacing the flame toward the grounded electrode (Ren et al., 2018; Tang et al., 2022). For AC electric fields, instabilities occur primarily at low frequencies (<10 Hz) (Tang et al., 2022), whereas at higher frequencies (50-500 Hz) they have been observed to increase flame temperature, suggesting a higher Damköhler
50 number and greater stability (Gan et al., 2015). While studies have shown that plasma suppresses the growth of soot particles (Cha et al., 2005; Ohisa et al., 1999; Su et al., 2018), the effect of plasma on the combustion synthesis of inorganic particles has not been studied. Furthermore, there have been no in-situ diagnostic investigation of aerosol formation during PAC, highlighting the gap in current research.

55 Particle formation in combustion systems has been widely studied and it is well established that this process occurs in several stages including nucleation, coagulation, condensation, and sintering. Research on particle formation in flame systems has primarily focused on inorganic particles and hydrocarbon soot. During the particle formation in combustion, reactants undergo chemical transformation to produce molecules needed for nucleation. These product molecules, under super saturated conditions, form stable clusters that grow further through coagulation and condensation, facilitated by collisions with other particles and molecules (Pratsinis, 1998). Most of these initial stages of particle formation and growth
60 occur in the size scale below 3 nm, which is a challenging size range to be characterized. Using a high-resolution differential mobility analyzer (HRDMA) which suppresses the diffusion losses of particles in the sub 3 nm size range, Wang et al., (2017a) studied particle formation with titania and silica-based precursors. They found several discrete peaks showing us the existence of stable nucleates with mobility diameter in the range of 0.9 – 1.7 nm. Moreover, most of the incipient particles measured in the system are charged due to the chemical ionization in the flame (Wang et al., 2017b). The study of nickel



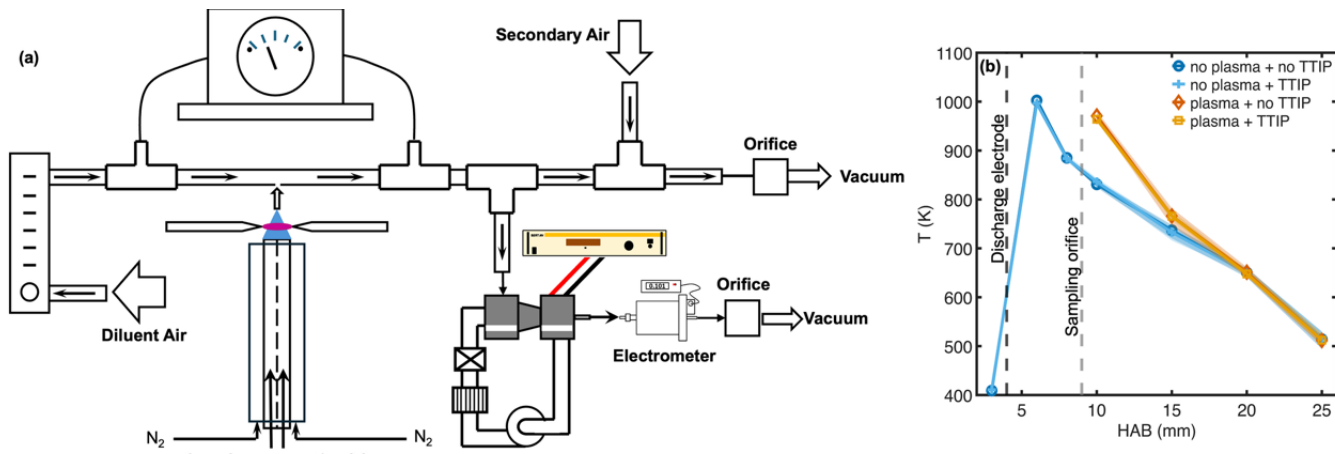
65 oxide nanoparticles formed during combustion found that the coagulation efficiency of particles below 5 nm is orders of magnitude lower than unity, suggesting that for inorganic particles, coagulation driven growth is more significant in size ranges above 5 nm (Carbone et al., 2008). Such growth is also supported by in-situ laser diagnostic results from phase-selective LIBS of flame-synthesized nanoparticles, where the atomic emission signal saturates at approximately 6 nm (Ren et al., 2015). Regarding the formation of soot particles in combustion, Carbone et al., (2019, 2021) analyzed the clusters in the
70 atmospheric pressure inlet time-of-flight (APi-TOF) mass spectrometer (MS) (Junninen et al., 2010). Their research (Carbone et al., 2019) examined the clusters for mass-to-charge ratio up to 2000 Thompson and found that the charging of flame pyrolysis products likely occurs by protonation/deprotonation mechanism. Another study examining weakly bound hydrocarbon molecular clusters found that clusters with masses lighter than 400 Daltons (Da), where one Dalton is defined as 1/12th the mass of a carbon-12 atom, and having a C/H ratio between 2 and 3 were responsible for the inception of soot
75 (Carbone et al., 2021).

The process of particle formation and growth is strongly influenced by interactions between particles, charged carriers, and the surrounding electric field. Flames, being weak plasma systems, contain relatively high concentrations of charge carriers, such as ions and electrons (Fialkov, 1997). Several studies have leveraged this characteristic by applying external electric fields to manipulate the movement of charge carriers (Altendorfner et al., 2011; Belhi et al., 2010; Kammler et al.,
80 2003; Saito et al., 1999; Xiong et al., 2017; Zhao et al., 2008). The introduction of plasmas into the flames in PAC will significantly enhance particle interactions with charged carriers and electric fields. As opposed to moving the charge carriers in a flame using electric fields, introducing plasma into the flame allows for more extensive modifications of reaction kinetics (Ju and Sun, 2015a, b). Introducing plasma into the flame will significantly increase the concentration of charges and radicals. Depending on the type of plasma, the electron concentration can reach up to 1023 m⁻³, with electron energies
85 ranging from 0.8 eV to 10 eV. In addition to high-energy electrons, there is also high concentration of radicals such as NO, O₃, O, H, and OH (Ju and Sun, 2015a). Although each of these components plays a role in enhancing the flame, the most important component is the high-energy electron, due to its ability to initiate or alter reactions. Li et al., (2019) discovered that in the corona discharge, the electron temperature around the electrode can increase by 350% and the concentration of plasma-related species (including radicals and charge carriers) can increase by 400%. These electrons and charged species
90 are generated on the tip/edge of the electrodes, which are placed outside the high-temperature region, and how they are introduced into the flame depends on the type of power source used to generate the discharge (Ohisa et al., 1999). If a direct current (DC) power source is used, the charged species are introduced to the flame via the ionic wind and in the case of an AC power source, the charged species enter the flame via diffusion. The concentration of charged species introduced into the flame varies significantly between DC and AC power sources, with DC powered corona discharges delivering a higher
95 concentration (Ohisa et al., 1999). The difference in charged species concentration leads to different effects on particle formation within flame.

Although studies have investigated PAC on its role in enhancing flame stability and efficiency, only a few have focused specifically on particle formation and growth. Vemury and Pratsinis, (1995) examined the TiO₂ particles produced in a DC



corona discharge-assisted diffusion flame reactor. They reported that the corona discharge reduces the particle residence time 100 in the high-temperature region due to ionic wind effects, reducing the particle diameter. Similarly, Ohisa et al., (1999) applied DC and AC corona discharges to a sooting propane turbulent diffusion flame and reported a significant reduction in soot. This reduction was attributed to the charging of incipient soot particles and decreased concentration of ions like $C_3H_3^+$, which act as precursors in the ionic mechanism of soot formation. Despite these findings, further research is needed to obtain 105 more mechanistic understanding of particle formation and growth in PAC under different plasma and flame configurations. This study aims to investigate the impact of introducing the corona discharge into a flame on the size distribution of inorganic particles. A high-voltage AC power source is used to generate corona discharges of varying powers across a premixed methane-air flame. The flame is fed with Ti and Si-based precursors to generate Ti-containing or Si-containing nanoparticles. In this study, we use a HRDMA combined with an electrometer to obtain the size distribution of particles 110 (Fernández de la Mora and Kozlowski, 2013) in the size range 1 to 10 nm. We examined the effect of corona discharge on the size distribution of Ti-containing and Si-containing particles under varying plasma powers, precursor feed rates, and for both positively and negatively charged particles. We further used different charging models to examine the impact of plasma on particle formation. The methods and results of this study can be used to design nanomaterials synthesis platforms using 115 PAC.



115 **Figure 1:** (a) Schematic of the experimental apparatus. (b) Temperature profile of flames under different plasma and synthesis precursor conditions. The feed rate of TTIP is 19 mg h^{-1} for temperature profile measure, and the plasma power is 125 W.

2 Methods

2.1 Flame and Particle Analysis

The schematic diagram of the combustion system used is shown in Fig. 1a, which is similar to that presented in Bagya 120 Ramesh and Wang (2024). We used a premixed flame sustained above a tube burner. The burner was built using two 316L



stainless steel tubes with outer diameters of 6.35 mm and 12.7 mm, which were placed concentrically. A stream of N₂ at a flow rate of 0.6 lpm was introduced through the space between the two tubes as a sheath. CH₄ and O₂ were introduced to the inner tube at flow rates of 0.09 lpm and 0.18 lpm, respectively, to provide a stoichiometric flame. Particle synthesis precursors, titanium isopropoxide (TTIP) or tetraethyl orthosilicate (TEOS), were added to the gas mixture to generate Ti-containing and Si-containing particles. We chose to study the formation of Ti-containing and Si-containing particles, as they are among the most important inorganic oxides produced by combustion, which are used extensively in paints (Braun et al., 1992), catalysts (Kim et al., 2011; Niu et al., 2014), solar cells (Thimsen et al., 2008), carbon-based product manufacturing (Spicer et al., 1998), and drug delivery systems (Alavi et al., 2022). The precursors are liquid and were introduced into the reactant stream in the gaseous phase by bubbling N₂ through their respective liquid media. We could introduce different amounts of precursors by varying the flow rate of N₂ passed through the precursor (calibrated using a bubble flow meter, Sensidyne Gilian Gilibrator) and the temperature of the precursor liquid. The amount of TTIP and TEOS introduced was calculated by obtaining their saturation vapor pressures from Eq. (1) and Eq. (2), respectively (Hee Dong Jang, 1999; Siefering and Griffin, 1990).

$$\log_{10}(P_{eq}) = 9.837 - \frac{3193.7}{T} \quad (1)$$

$$135 \quad \ln P = 19.3 - \frac{5555}{T} \quad (2)$$

We used precursor feed rates of 9.6, 19.2, 28.7, 38.4, and 48 mg h⁻¹ for TTIP and 60, 80, and 100 mg h⁻¹ for TEOS when synthesizing Ti-containing and Si-containing particles. We obtained the above feed rates by introducing N₂ through TTIP at a flow rate of 0.1, 0.2, 0.3, 0.4, and 0.5 lpm. Similarly, for TEOS, we used N₂ flow rate of 0.03, 0.04, and 0.05 lpm. Additional N₂ was introduced to the flame, so the O₂ and N₂ molar ratio was maintained at 1:3.76, simulating the air composition. Based on the highest feed rate of both precursors, 48 mg h⁻¹ for TTIP and 100 mg h⁻¹ for TEOS, complete oxidation of TTIP would make the mixture ~0.7% fuel-rich relative to stoichiometric, while TEOS would make it ~1.3% fuel-rich. Because the flame remains close to stoichiometric conditions, there is little to no change in flame temperature, as shown in Fig. 1b. We should note that there might be trace amounts of carbon on generated particles due to slightly fuel-rich conditions. The particles formed from the flame are extracted and studied using a hole-in-a-tube (HiAT) type dilution sampling probe (Zhao et al., 2003), HRDMA, and a TSI 3068A electrometer. The HiAT dilution sampling probe is operated with zero air as the diluent, which is generated by a HEPA filter. Two streams of diluent air are provided to the sampling probe, one upstream (diluent air) and one downstream (secondary air) of the aerosol sampling inlet. The aerosol flow rate at the probe inlet above the flame is controlled by controlling the upstream and downstream airflow. The diluent air and secondary air used for the dilution sampling probe are supplied at a rate of ~31 lpm and 2 lpm.

150 Using the method in Zhao et al., (2003), we calculated the dilution ratio for this study, which is 152 after accounting for the thermal expansion of air. A single set of flow condition was used for all experiments. Flow rates in the dilution system were held constant to keep the dilution ratio and sampling conditions consistent across cases. The above ratio is a product of the dilution due to flow mixing and thermal expansion. Dilution due to flow mixing was obtained by measuring the ambient



particle concentration with and without dilution using a TSI model 3750 condensation particle counter and was found to be
155 45.3. Dilution due to thermal expansion was 3.36 from the ratio of aerosol sample temperature (1003 K) to that of dilution air (298 K). For our experiments, particles were sampled using a ¼ inch copper tube with a length of 0.88 m with 5.85 lpm of flow pass through. The number concentration detected by the electrometer was on the order of 10^5 cm^{-3} . After performing data inversion, as described in our previous work (Bagya Ramesh and Wang, 2024), which accounts for diffusional and penetration losses, the number concentration increased to the order of 10^{10} cm^{-3} . This result is expected, given the sub-10 nm
160 particle size range being sampled. The HRDMA was operated in series with a TSI 3068A electrometer. HRDMA used a sheath flow of 277.5 lpm and a sample flow rate of 5.85 lpm. The voltage of the central electrode was scanned from 0 V to 5000 V to obtain mobility diameters of particles up to a size of 8 nm. We should note that throughout this paper, the term particle size refers specifically to the mobility size. Mobility size differs from the actual particle diameter, as it is determined by the balance between drag forces and electrostatic forces acting on the particle in an electric field. The mobility size can be
165 related to the physical size, aerodynamic size, or the volumetric size of the aerosol particles (Larriba et al., 2011). However, these conversions require knowledge on the shape and density of the particles. The HRDMA was calibrated using the monodisperse tetra-alkyl ammonium halide ions (Ude and De La Mora, 2005), and we can convert mobility to mobility size based on the equation,

$$Z = Cne/3\pi\mu D_p \quad (3)$$

170 In Eq. (3), C is the Cunningham slip correction factor, n is the number of charges on the particle, e is the electronic charge, μ is the air viscosity, and D_p is the mobility size.

To generate the corona discharge, we used two tungsten electrodes placed 6 mm apart and 3 mm above the tube burner. The electrodes were provided by Thermo Scientific as 2 mm diameter Tungsten rods of purity 99.95% (metals basis). The high purity of the material ensured minimal corrosion even after using them for several hours. The tips of the electrodes were
175 sharpened to increase the intensity of electric field and facilitate gas breakdown. A high-voltage, high-frequency AC power supply (PVM400DELUX, HVC Capacitor Manufacturing Co., Ltd) was used as the power source. This AC power source has a variable output from 1 to 15 KV and from 20 to 50 kHz. For the experiments conducted in this study, we examined the corona discharge generated from this power source at two different operating conditions. One operating condition corresponds to the onset of the corona discharge (1.9 kV, 58.5 mA, 21.6 kHz), and the other operating condition corresponds
180 to the maximum power of the power supply (1.8 kV, 131.6 mA, 20.4 kHz). The major difference between the two conditions is the current through plasma, or the power of the plasma (56 W and 125 W). Since the power source is in high-frequency AC, ionic wind effects are minimized and can be ignored. Flame temperature was also measured in the presence of a corona discharge (at 125 W). To minimize plasma interference, the thermocouple probe was positioned at least 6 mm from the discharge electrode. Introducing the corona discharge increased flame temperature, an unexpected result given the non-
185 thermal nature of the corona discharge plasma. This effect can be attributed to elongation of the flame reaction zone observed in our experiment, which extended the high-temperature region. The resulting temperature rise may also influence particle formation and growth downstream. The experimental conditions used in this study are summarized in Table 1.



Table 1: Experimental plan for this study.

Task	Precursor	Corona discharge power
1	-	-
2	-	56 W and 125 W
3	TTIP (9.6 – 48 mg h ⁻¹)	-
4	TTIP (9.6 – 48 mg h ⁻¹)	56 W and 125 W
5	TEOS (60 – 100 mg h ⁻¹)	-
6	TEOS (60 – 100 mg h ⁻¹)	125 W

190

2.2 Estimating charging characteristics

The charging characteristics of plasma ions and electrons with particles were calculated to understand the role of charging in particle growth within such systems. We analyzed the diffusion and field charging effects of ions sampled under two conditions: flame only and PAC with a plasma power of 125 W. The diffusion charging effects were determined using Eq. 195 (4), while the field charging effects were calculated using Eq. (5) (Benjamin Y. H. Liu and Hsu-Chi Yeh, 1968; Friedlander, 2000).

$$n = (akT/\epsilon^2) \ln(1 + \pi\epsilon^2 c a N_0 t / kT) \quad (4)$$

$$n = n_s \pi N_0 \epsilon Z t / (\pi N_0 \epsilon Z t + 1) \quad (5)$$

In Eq. (4), a is the particle radius, c is the thermal speed of ions, N_0 is the concentration of ions far away from the particle, ϵ is the elementary unit charge, k is the Boltzmann's constant, t is the exposure time of the particle to unipolar ions, and T is the temperature in K. In Eq. (5), Z is the mobility diameter, n_s is the saturation charge, n is the charge of the particle. Although not directly used in Eq. (4), the value of the particle's dielectric constant (K) is required to calculate n_s . The saturation charge is calculated using Eq. (6), where E_0 is the intensity of applied electric field.

$$n_s = \{1 + 2[(K - 1)/(K + 2)]\} (E_0 a^2 / \epsilon) \quad (6)$$

205 We present here only the key equations used to calculate charge accumulation on particles, and the detailed steps for this calculation can be found elsewhere (Benjamin Y. H. Liu and Hsu-Chi Yeh, 1968; Friedlander, 2000). Assuming that the particles were mostly TiO₂ and SiO₂, the dielectric constants for these particles were taken as 30 and 3.9, respectively. All parameters used in Eqs. (4) and (5) were expressed in SI units. To estimate the exposure time of particles to ions, we calculated the gas flow velocity within the flame and the duration particles remain within the flame region. The volumetric 210 flow rate of the flame was calculated from CH₄, O₂, and N₂ feed rates to be $1.578 \times 10^{-5} \text{ m}^3 \text{ s}^{-1}$. Dividing the volumetric flow rate with the cross section of tube burner gave us a flow velocity of 0.498 m s^{-1} . The particles were assumed to be exposed to

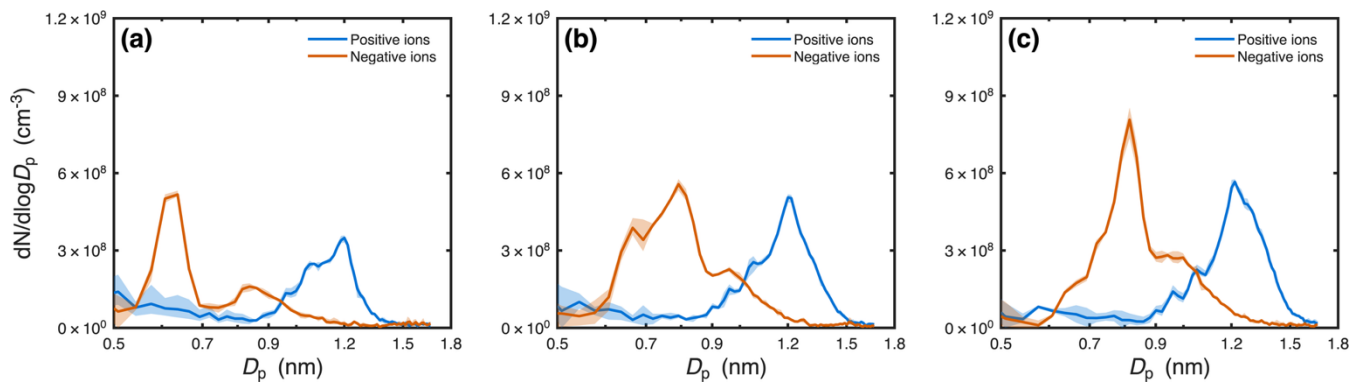


the ions only for the duration that they spent within the flame, which had a flame height of 6.35 mm. From the flame height and flow velocity, the exposure time of the particle was estimated to be 12.7 ms. These calculations assume that only neutral particles are charged through field charging.

215 3 Results and Discussion

3.1 Ions of flames vs plasma

Figure 2 shows the size distributions of positive and negative ions measured in the flame without plasma (Fig. 2a) and corona discharge-assisted combustion (Figs. 2b and 2c) without particle-forming precursors. From Fig. 2a, the negative ions exhibit bimodal peaks at 0.6 nm and 0.8 nm for the flame without the corona discharge condition, whereas the positive ions display a broader unimodal peak at 1.2 nm. The size distributions of flame-generated ions are similar to those reported in a previous study (Bagya Ramesh and Wang, 2024), which are dominated by charge carriers below 2 nm. After introducing the corona discharge into the flame, the positive ion size distribution does not change significantly with regard to size (Figs. 2b and 2c). The peak size for the positive ions stays at around 1.2 nm under corona discharge powers of 56 W and 125 W. However, there is a significant increase in ion concentration, with an increase of 45% and 62% for corona discharge powers of 56 W and 125 W. The relative consistency of the mobility sizes for positive ions with and without the corona discharge implies that positive ionic species are similar under all three conditions. At the same time, the increase in concentration indicates that the corona discharge enhances the rate of reactions responsible for forming these ions from both combustion and corona discharge. However, the ion concentrations under corona discharge do not scale with the plasma power.



230 **Figure 2: (a) The size distribution of positive and negative ions under flame without plasma. Positive ions have a unimodal peak at 1.2 nm whereas the negative ions have a bimodal peak at 0.6 nm and 0.8 nm; (b) The size distributions of positive and negative ions under plasma power of 56 W. Positive ions retain the unimodal peak at 1.2 nm with higher concentration whereas the negative ions have a wider peak at 0.8 nm; and (c) The size distributions of positive and negative ions under plasma power of 125 W. Positive ions retain the unimodal peak at 1.2 nm and the negative ions have a sharper peak at 0.8 nm. For each experimental condition, the size distribution was obtained by scanning high voltage from 0V to 5000V three times. The shaded region shows the range (minimum to maximum) for number concentration at any given size.**



Regarding the negative ion size distributions, in a flame assisted by a corona discharge at 56 W, the peak at 0.6 nm slightly diminishes, while the peak at 0.8 nm was enhanced (Fig. 2b). At the same time, we see a peak emerge at 1.0 nm. This trend continues when the corona discharge power increases to 125 W (Fig. 2c), with a more substantial peak at 0.8 nm and the peak at 1.0 nm. This suggests that the introduction of a corona discharge promotes reactions that generate ions with a mobility diameter of 0.8 nm in the flame without plasma. Overall, we observe that the corona discharge has a stronger influence on the formation of negative ions than on the formation of positive ions.

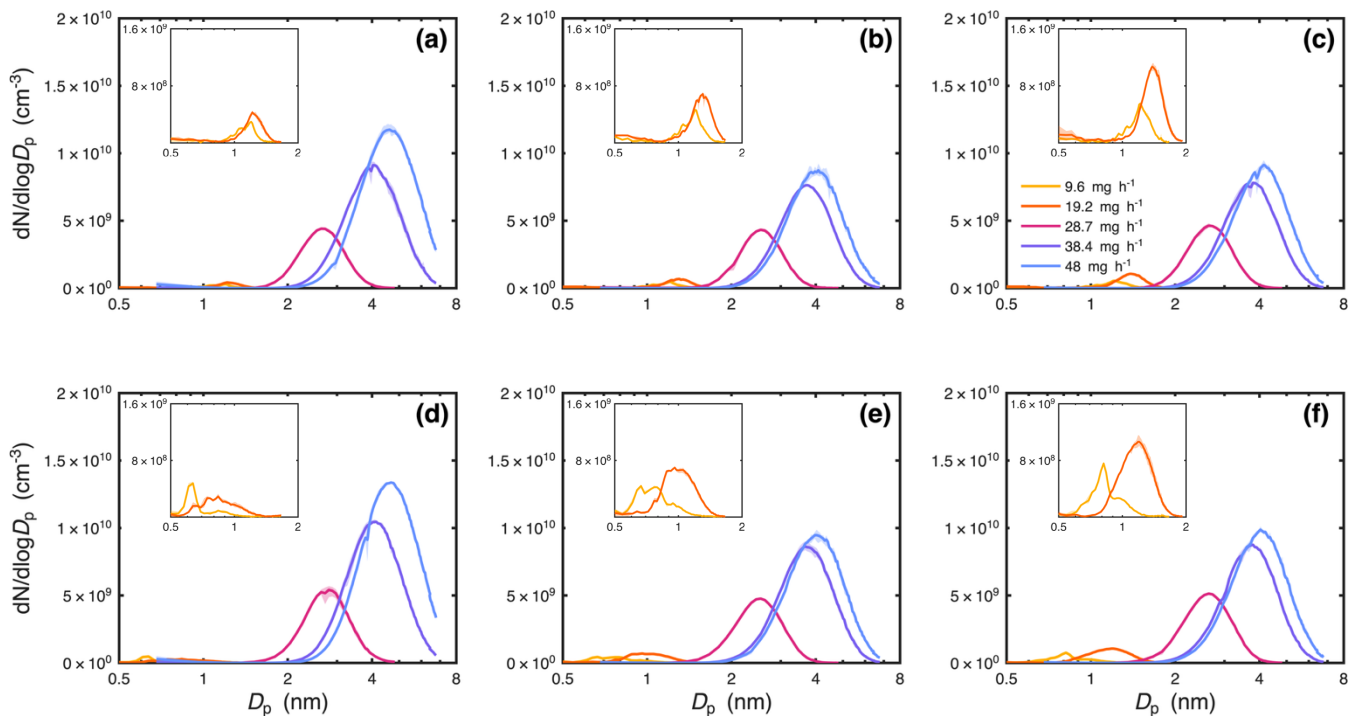


Figure 3: (a), (b), and (c) are size distribution of positively charged Ti-containing clusters without plasma, with plasma of power 56 W, and with plasma of power 125 W respectively. Similarly, (d), (e), and (f) are the size distributions of negatively charged Ti-containing clusters without plasma, with plasma power 56 W, and with plasma power 125 W respectively. The inset plots show the size distributions of two lowest flowrates, 9.6 and 19.2 mg h^{-1} . The shaded region shows the range for number concentration at any given size.

3.2 Influence of corona discharge on size distribution of particles

Figure 3 shows the size distribution of Ti-containing particles forming under different TTIP feed rates and different corona discharge conditions. Overall, as the feed rate of TTIP increases from 9.6 mg h^{-1} to 48 mg h^{-1} , we observe an increase in the concentration of Ti-containing particles, which results in particles growing to larger sizes by coagulation. Due to the low concentration of aerosols under low precursor feed rates, the size distribution of Ti-containing for TTIP feed rates 9.6 mg h^{-1} and 19.2 mg h^{-1} are presented using inset plots. Compared to the flame without plasma (Figs. 3a and 3d), the size distribution of particles formed with plasma shifts toward larger sizes under low precursor concentrations and shifts toward smaller sizes under high precursor concentrations. This shift can be seen clearly from Figs. 5a and 5b, which shows the effect of plasma



on the mode size of Ti-containing particle size distribution as percentage change with respect to the mode size of Ti-containing particles generated from non-plasma combustion.

Under the lower TTIP feed rates of 9.6 mg h^{-1} and 19.2 mg h^{-1} , in a corona discharge-assisted combustion atmosphere, we observe that particle concentration is promoted compared to flame without plasma. This shift is visible from the size distribution of positively charged clusters in the inset plots of Figs. 3a to 3c. A similar effect appears for the size distribution of negatively charged clusters, as seen in the inset plots of Figs. 3d to 3f. For positively charged clusters, the concentration of the flame-generated particles under 125 W plasma increases by 86% and 150% for the feed rate of 9.6 mg h^{-1} and 19.2 mg h^{-1} , respectively, compared to the condition without plasma (Fig. 3c against Fig. 3a). The increase in particle concentration also promotes the coagulation growth of the particles, where the particle size from a feed rate 19.2 mg h^{-1} of TTIP under 125 W plasma increases by 14% to a mode diameter of 1.38 nm compared to 1.21 nm for the condition without plasma. Similarly, for negatively charged clusters, the concentration of the flame-generated particles under 125 W plasma increases by 59% and 265% for the feed rate of 9.6 mg h^{-1} and 19.2 mg h^{-1} , respectively, compared to the condition without plasma (Fig. 3f against Fig. 3d). The mode mobility diameter increases by 28% to 0.81 nm and by 42% to 1.18 nm for a feed rate of 9.6 mg h^{-1} and 19.2 mg h^{-1} , respectively, under 125 W plasma compared to the condition without plasma.

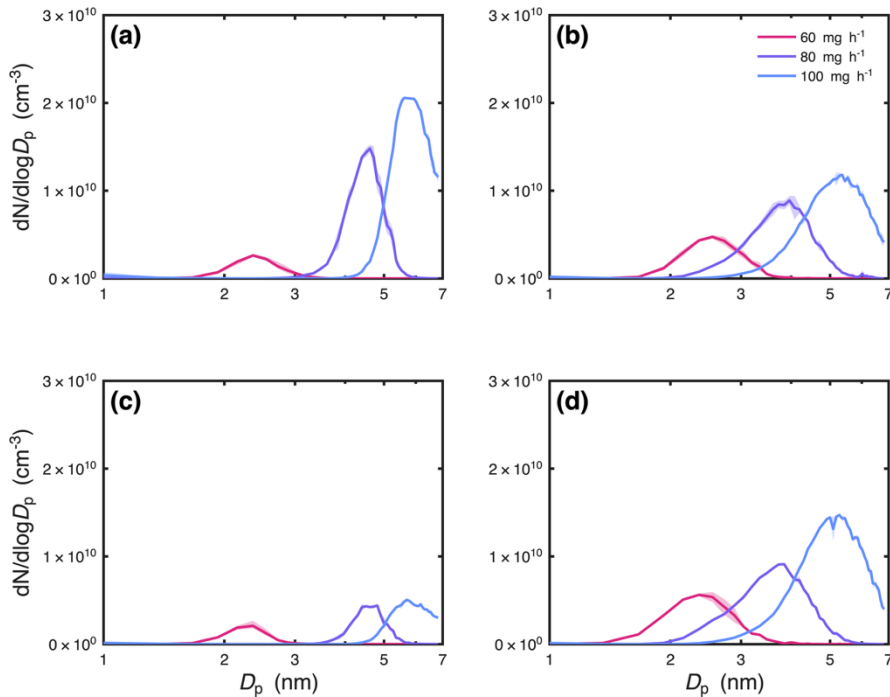
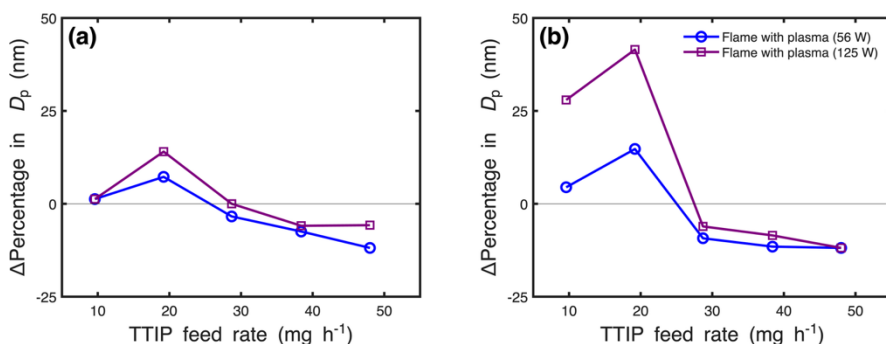


Figure 4: Size distributions of positively charged Si-containing clusters (a) without plasma and (b) with plasma of power 125 W. Size distributions of negatively charged Si-containing clusters (c) without plasma and (d) with plasma of power 125 W. For each experimental condition, the size distribution was obtained by scanning high voltage from 0V to 5000V three times. The shaded region shows the range for number concentration at any given size.



275 At higher TTIP feed rates of 28.7, 38.4, and 48 mg h^{-1} in the corona discharge-assisted combustion atmosphere, we observe the Ti-containing particle size shifting towards a smaller size than compared to a flame without plasma. Under 125 W plasma, the mode mobility diameter of the positively charged clusters decreases by 6% to 3.8 and 4.3 nm for both 38.4 mg h^{-1} and 48 mg h^{-1} but remained unchanged at 2.63 nm for 28.7 mg h^{-1} (Fig. 3c against Fig. 3a). The mobility diameter decreases for the negatively charged clusters by 6%, 9%, and 12% to 2.6 nm, 3.8 nm, and 4 nm, respectively (Fig. 3f against 280 Fig. 3d). We also examined the effect of the power of corona discharge on size distribution. We find that promotion and suppressive effects remain for plasmas of both powers, but the promotional effects are stronger for a corona discharge with the higher power of 125 W.

285 Figure 4 shows the size distribution of particles formed using TEOS and the corresponding feed rates. Like the size distribution of particles formed using TTIP, the particles generated show both promotional and suppressive effects on particle growth depending on the precursor feed rate. At a lower TEOS feed rate of 60 mg h^{-1} , we observe a higher concentration of particles with corona discharge-assisted combustion (Fig. 4b and 4d) compared to the flame without plasma (Fig. 4a and 4c). The size of the formed particles also increases due to the presence of the plasma. For the feed rate of 60 mg h^{-1} , we see the mode mobility diameter increase by 8% to 2.54 nm (Fig. 4b against 4a). For higher TEOS feed rates of 80 mg h^{-1} and 100 mg h^{-1} , we observe the Si-containing particle size shifting towards a smaller mode mobility size with corona 290 discharge-assisted combustion (Fig. 4b and 4d) compared to the flame without plasma (Fig. 4a and 4c). The mode mobility diameter of positively charged clusters decreases by 14% to 4 nm and by 4.5% to 5.4 nm for 80 mg h^{-1} and 100 mg h^{-1} , respectively, in the presence of plasma. Meanwhile, the mode mobility diameter of negatively charged clusters decreases by 20.1% to 3.85 nm and by 7.5% to 5.27 nm, respectively. Though we saw suppressive effects on mode mobility diameter with both, 56 W plasma and 125 W plasma, we didn't see the suppressive effects scale with plasma power.



295

Figure 5: (a) and (b) show the effects that the corona discharge has on the mode size of positively and negatively charged Ti-containing particles, respectively. In both plots (a) and (b), the line at $y = 0$ is the reference to Ti-containing particles generated from non-plasma combustion.

3.3 Mechanism underlying the influence of corona discharge on particle formation

300 Overall, we observed that when we introduced the high-frequency AC corona discharge in the flame, particle formation and growth were promoted under low precursor feed rates but were suppressed under higher precursor feed rates (Fig. 5) with



respect to the particles generated from non-plasma combustion. The promotion effect under the low precursor feed rates (TTIP feed rates below 19.2 mg h^{-1} and TEOS feed rate below 60 mg h^{-1}) was likely due to the introduction of the plasma-generated ions that had a higher or similar concentration compared to the synthesized particles, which could coagulate and form larger particles. It is also possible that the introduction of the ions leads to ion-induced nucleation, where ions in nucleating vapors can enhance nucleation rates (Adachi et al., 1992; Lovejoy et al., 2004; Yang et al., 2024). This enhancement has been reported in previous studies on the particle formation kinetics of TiO_2 and SiO_2 particles (Adachi et al., 2004; Wang et al., 2015). Beyond the effect of ions in increasing nucleation rates, the presence of an electron-rich atmosphere has also been shown to promote the formation of particle nuclei at lower supersaturation levels, thereby further enhancing the nucleation rate (Vishnyakov et al., 2011). We start observing the suppression of particle growth at higher TTIP feed rates of 28.7, 38.4, and 48 mg h^{-1} . A similar trend is seen at higher TEOS feed rates of 80 and 100 mg h^{-1} . In case of both precursors, the peak mobility diameter decreased in the presence of a corona discharge. We should note that the sampling height is fixed in this work. Therefore, the measurement under different precursor feed rates captures different stages of growth for the nanoparticles. Ion-induced nucleation likely also promoted particle formation at the larger precursor concentration, which occurred before the particles are sampled. The fact that the plasma suppressed particle formation under the higher precursor concentration indicates that the suppression effect is stronger than the promotion effect in particle growth during PAC under higher precursor feed rates.

Here, we further use different models to examine the effect of plasma on aerosol charging. We mainly focus on the suppression effect of the plasma on particle formation and growth under higher precursor feed rates, which is relevant in gas-phase particle synthesis and pollution control, where particles of relatively larger sizes are formed under high precursor feed rates. Due to the high concentration of ions and in PAC atmosphere, the nascent particles are bound to be charged by the charge carriers. Understanding such charging is crucial as it determines inter-particle dynamics in the flame and in the downstream flow region. Particles in PAC and flame systems are mainly charged by collisional mechanisms, where the charge carriers impart charges by colliding with particles.

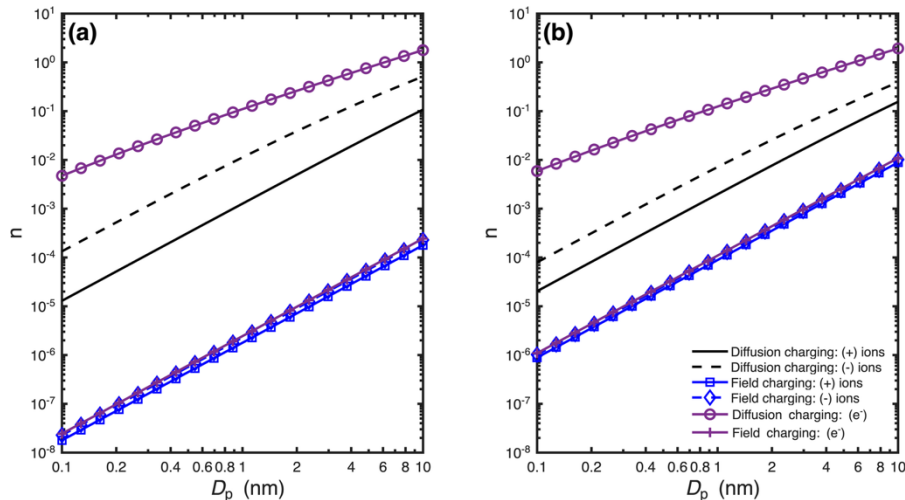




Figure 6: Shows the charge acquired by Ti-containing particles with a dielectric constant of 30 from diffusion and field charging in (a) flame only condition and (b) PAC with a plasma of power 125 W.

Figure 6 shows the charge accumulated on the Ti-containing particles due to diffusion and field charging effects in all operating conditions. The charges accumulated on Si-containing particles are very similar to those accumulated by Ti-containing particles, except for Si-containing particles acquiring less charge from field charging due to their lower dielectric constant of 3.9. The charge accumulated by Si-containing particles is given in Fig. S1. By comparing Fig. 6a and Fig. 6b, we can see that with the introduction of a corona discharge, the charges accumulated due to diffusion charging in PAC with plasma of power 125 W are 8% to 57% higher than the charges that are accumulated in flame only condition, showing that the diffusion charging is enhanced. Even though our earlier measurements showed that generating a corona discharge would introduce ions with less mobility than the ones in flame only condition (Fig. 2c). The enhancement in diffusion charging despite PAC ions having less mobility than flame ions is likely due to the higher concentration of PAC ions. We observe that this phenomenon is stronger with enhancement of 25% - 57% at a smaller particle size, $D_p = 0.1$ nm, than the enhancement of 8% - 45% at a bigger particle size, $D_p = 10$ nm.

Similarly, if we compare Fig. 6a and Fig. 6b for charge accumulated due to field charging, we see that for the condition with plasma of power 125 W, the charge accumulated is ~ 48 times higher than in the flame only condition. From Fig. 6, we also see that particles accumulate more negative charge than they do positive charge. Such preferential charging is likely due to the higher mobility and lower mass of negative ions than that of positive ions. Though field charging is significantly enhanced due to strong electric field in PAC, diffusion charging is still dominant in the observed size range (1-10 nm). Field charging effects become more dominant with the increase in particle size as more field lines intersect with the particle surface.

By introducing corona discharge into the flame, we increase the concentration of electrons. It is important to note that the electrons generated in the corona discharge or the flame have very high mobility and a small size, which cannot be measured by HRDMA. Here, we assume that the number of electrons is the same as the concentration of positive ions and calculate the diffusion and field charging effects of electrons. However, in reality, the electron concentration is likely much higher in plasma-assisted combustion (PAC) than in the flame-only condition. A higher electron concentration results in a greater accumulation of negative charges on particles. From Fig. 6b, we can see that the diffusion charging due to electrons is several orders of magnitude greater than that due to positive and negative ions. This higher charging capability is due to their extremely high mobility ($4000 \text{ cm}^2 \text{ V}^{-1} \text{ s}^{-1}$) (Bisetti and El Morsli, 2012) and low mass ($9.11 \times 10^{-31} \text{ kg}$), enabling electrons to diffuse much faster than heavier ions in the considered PAC system. The combined effects of high diffusion charging by electrons and preferential negative charging of particles will result in a greater fraction of particles being charged negatively. As a result, particle formation and growth of flame-generated particles will be suppressed due to electrostatic repulsion. To fully understand the effect of plasma on combustion synthesis of nanomaterials, in situ measurements need to be combined with ex-situ imaging and chemical analysis. However, imaging analysis, such as transmission electron microscopy (TEM) and atomic force microscopy (AFM), are challenging at the sub 5 nm size range, as they require the capture and analysis of



360 highly diffusive particles. Similar challenges arise when one tries to sample particles for chemical analysis (Botero et al., 2016; Commodo et al., 2019; Fang et al., 2014; Schulz et al., 2019; Veronesi et al., 2022). Therefore, future work is needed to understand the influence of plasma on particle formation and growth via more comprehensive techniques.

4 Conclusion

In this study, we introduced a corona discharge in a flame using a high-voltage AC power source. Upon scanning the ion size 365 distributions using HRDMA, we found out that we are not generating significant quantities of new ionic species; we are only increasing the concentration of the existing flame ions. Though we do not see any significant changes to the mobility diameter for the positive ions, we do see a shift in the size distribution relating to the negative ions. We also examined the effect of corona discharge on particle formation by studying the effect on size distribution of particles when we introduce synthesis precursors (TTIP and TEOS) to the flame. From our results we found that the effect of corona discharge on particle 370 formation depends on the synthesis precursor concentration. Particle formation and growth were promoted under low precursor feed rates but suppressed under higher precursor feed rates. The promotion effect under the low precursor feed rates was likely due to the introduction of the plasma-generated ions that have a higher or similar concentration compared to the synthesized particles, which can coagulate and form larger particles. It is also possible that the introduction of the ions leads to ion-induced nucleation, where ions in nucleating vapors can enhance nucleation rates. The suppression effect of the 375 corona discharge on particle formation and growth is likely due to the high diffusion charging due to electrons and preferential negative charging of particles due to the higher mobility of the negative ions. We also observe that in corona discharge assisted combustion, field charging is greatly enhanced. The findings of this study help us understand the effect of plasmas on particles during combustion synthesis of nanoparticles and pollution control using PAC. We should note that mobility analysis alone is insufficient to fully resolve plasma effects on particle formation; complementary offline imaging 380 and chemical characterization of newly formed particles would clarify mechanistic insight and improve the control of particle formation in PAC.

Data availability. The data associated with this article can be made available by the corresponding author upon request.

Appendix A: Nomenclature

- a Particle radius, m
- c Mean thermal speed of ions, m s⁻¹
- E_0 Intensity of applied electric field, V m⁻¹
- k Boltzmann's constant, 1.38×10^{-23} J K⁻¹
- n_s Saturation charge on particle, elementary units



N Concentration of ions, ions m^{-3}
 N_0 Concentration of ions at a large distance from particle, ions m^{-3}
 t Time, s
 T Absolute temperature, $^{\circ}\text{K}$
 Z Electrical mobility, $\text{m}^2 \text{V}^{-1} \text{s}^{-1}$
 ϵ Elementary unit of charge, $1.602 \times 10^{-19} \text{ C}$

Author contributions. CRediT: Chanakya Bagya Ramesh: Investigation, Data curation, Formal analysis, Writing – original
385 draft, Methodology, Visualization. Frank Daoru Han: Writing – review & editing, supervision. Yang Wang: Conceptualization, Funding Acquisition, supervision, writing – review & editing.

Competing interests. The authors declare that they have no known competing financial interests or personal relationships that could have appeared to influence the work reported in this article.

Acknowledgements. This work is supported by National Science Foundation award 2132655.

390 References

Adachi, M., Okuyama, K., and Seinfeld, J. H.: Experimental studies of ion-induced nucleation, *J Aerosol Sci*, 23, 327–337, [https://doi.org/10.1016/0021-8502\(92\)90002-D](https://doi.org/10.1016/0021-8502(92)90002-D), 1992.

Adachi, M., Kusumi, M., and Tsukui, S.: Ion-induced nucleation in nanoparticle synthesis by ionization chemical vapor deposition, *Aerosol Science and Technology*, 38, 496–505, <https://doi.org/10.1080/02786820490460734>, 2004.

395 Alavi, M., Hamblin, M., Mozafari, M., Rose Alencar de Menezes, I., and Douglas Melo Coutinho, H.: Surface modification of SiO_2 nanoparticles for bacterial decontaminations of blood products, *Cellular, Molecular and Biomedical Reports*, 2, 87–97, <https://doi.org/10.55705/cmbr.2022.338888.1039>, 2022.

Altendorfner, F., Kuhl, J., Zigan, L., and Leipertz, A.: Study of the influence of electric fields on flames using planar LIF and PIV techniques, *Proceedings of the Combustion Institute*, 33, 3195–3201, <https://doi.org/10.1016/j.proci.2010.05.112>, 2011.

400 Bagya Ramesh, C. and Wang, Y.: Ions Generated from a Premixed Methane-Air Flame: Mobility Size Distributions and Charging Characteristics, *Combustion Science and Technology*, 196, 4041–4056, <https://doi.org/10.1080/00102202.2023.2203818>, 2024.



Belhi, M., Domingo, P., and Vervisch, P.: Direct numerical simulation of the effect of an electric field on flame stability, 405 Combust Flame, 157, 2286–2297, <https://doi.org/10.1016/j.combustflame.2010.07.007>, 2010.

Benjamin Y. H. Liu and Hsu-Chi Yeh: On the Theory of Charging of Aerosol Particles in an Electric Field, *J Appl Phys*, 39, 1396–1402, [https://doi.org/10.1016/0021-9797\(69\)90368-3](https://doi.org/10.1016/0021-9797(69)90368-3), 1968.

Bisetti, F. and El Morsli, M.: Calculation and analysis of the mobility and diffusion coefficient of thermal electrons in 410 methane/air premixed flames, *Combust Flame*, 159, 3518–3521, <https://doi.org/10.1016/j.combustflame.2012.08.002>, 2012.

Botero, M. L., Adkins, E. M., González-Calera, S., Miller, H., and Kraft, M.: PAH structure analysis of soot in a non-premixed flame using high-resolution transmission electron microscopy and optical band gap analysis, *Combust Flame*, 164, 250–258, <https://doi.org/10.1016/j.combustflame.2015.11.022>, 2016.

Bradley, D. and Nasser, S. H.: Electrical Coronas and Burner Flame Stability, *Combust Flame*, 55, 53–58, 415 [https://doi.org/10.1016/0010-2180\(84\)90148-2](https://doi.org/10.1016/0010-2180(84)90148-2), 1984.

Braun, J. H., Baidins, A., and Marganski, R. E.: TiO₂ pigment technology: a review, *Prog Org Coat*, 20, 105–138, [https://doi.org/10.1016/0033-0655\(92\)80001-D](https://doi.org/10.1016/0033-0655(92)80001-D), 1992.

Carbone, F., Barone, A. C., De Filippo, A., Beretta, F., D'Anna, A., and D'Alessio, A.: Coagulation and Adhesion of 420 Nanoparticles generated in flame from droplets of Nickel Nitrate aqueous solutions, *Chem Eng Trans*, 16, 87–94, 2008.

Carbone, F., Canagaratna, M. R., Lambe, A. T., Jayne, J. T., Worsnop, D. R., and Gomez, A.: Exploratory analysis of a soot premixed flame via on-line high resolution (APi-TOF) mass spectrometry, *Proceedings of the Combustion Institute*, 37, 919–926, <https://doi.org/10.1016/j.proci.2018.08.020>, 2019.

Carbone, F., Canagaratna, M. R., Lambe, A. T., Jayne, J. T., Worsnop, D. R., and Gomez, A.: Detection of weakly bound 425 clusters in incipiently sootting flames via ion seeded dilution and collision charging for (APi-TOF) mass spectrometry analysis, *Fuel*, 289, 119820, [https://doi.org/https://doi.org/10.1016/j.fuel.2020.119820](https://doi.org/10.1016/j.fuel.2020.119820), 2021.

Cha, M. S., Lee, S. M., Kim, K. T., and Chung, S. H.: Soot suppression by nonthermal plasma in coflow jet diffusion flames using a dielectric barrier discharge, *Combust Flame*, 141, 438–447, <https://doi.org/10.1016/j.combustflame.2005.02.002>, 2005.

Commodo, M., Kaiser, K., De Falco, G., Minutolo, P., Schulz, F., D'Anna, A., and Gross, L.: On the early stages of soot 430 formation: Molecular structure elucidation by high-resolution atomic force microscopy, *Combust Flame*, 205, 154–164, <https://doi.org/10.1016/j.combustflame.2019.03.042>, 2019.

Ehn, A., Petersson, P., Zhu, J. J., Li, Z. S., Aldén, M., Nilsson, E. J. K., Larfeldt, J., Larsson, A., Hurtig, T., Zettervall, N., and Fureby, C.: Investigations of microwave stimulation of a turbulent low-swirl flame, *Proceedings of the Combustion Institute*, 36, 4121–4128, <https://doi.org/10.1016/j.proci.2016.06.164>, 2017.

Fang, J., Wang, Y., Attoui, M., Chadha, T. S., Ray, J. R., Wang, W. N., Jun, Y. S., and Biswas, P.: Measurement of Sub-2 435 nm clusters of pristine and composite metal oxides during nanomaterial synthesis in flame aerosol reactors, *Anal Chem*, 86, 7523–7529, <https://doi.org/10.1021/ac5012816>, 2014.



Fernández de la Mora, J. and Kozlowski, J.: Hand-held differential mobility analyzers of high resolution for 1-30nm particles: Design and fabrication considerations, *J Aerosol Sci*, 57, 45–53,
440 https://doi.org/10.1016/j.jaerosci.2012.10.009, 2013.

Fialkov, A. B.: Investigations on ions in flames, *Prog Energy Combust Sci*, 23, 399–528, https://doi.org/10.1016/s0360-1285(97)00016-6, 1997.

Friedlander, S. K.: *Smoke, dust, and haze*, Oxford university press, New York, 2000.

Galley, D., Pilla, G., Lacoste, D., Ducruix, S., Lacas, F., Veynante, D., and Laux, C. O.: Plasma-Enhanced Combustion of a
445 Lean Premixed Air-Propane Turbulent Flame using a Nanosecond Repetitively Pulsed Plasma, in: 43rd AIAA Aerospace Sciences Meeting and Exhibit, 1193, https://doi.org/10.2514/6.2005-1193, 2005.

Gan, Y., Luo, Y., Wang, M., Shi, Y., and Yan, Y.: Effect of alternating electric fields on the behaviour of small-scale laminar diffusion flames, *Appl Therm Eng*, 89, 306–315, https://doi.org/10.1016/j.applthermaleng.2015.06.041, 2015.

De Giorgi, M. G., Ficarella, A., Sciolti, A., Pescini, E., Campilongo, S., and Di Lecce, G.: Improvement of lean flame
450 stability of inverse methane/air diffusion flame by using coaxial dielectric plasma discharge actuators, *Energy*, 126, 689–706, https://doi.org/10.1016/j.energy.2017.03.048, 2017.

Nanotechnology and nanomaterials market: https://www.grandviewresearch.com/industry-analysis/nanotechnology-and-nanomaterials-market, last access: 22 June 2025.

Hee Dong Jang: Generation of silica nanoparticles from tetraethylorthosilicate (TEOS) vapor in a diffusion flame, *Aerosol
455 Science and Technology*, 30, 477–488, https://doi.org/10.1080/027868299304516, 1999.

Ju, Y. and Sun, W.: Plasma assisted combustion: Dynamics and chemistry, *Prog Energy Combust Sci*, 48, 21–83,
https://doi.org/10.1016/j.pecs.2014.12.002, 2015a.

Ju, Y. and Sun, W.: Plasma assisted combustion: Progress, challenges, and opportunities, *Combust Flame*, 162, 529–532,
https://doi.org/10.1016/j.combustflame.2015.01.017, 2015b.

Junninen, H., Ehn, M., Petäjä, Luosujärvi, L., Kotiaho, T., Kostiainen, R., Rohner, U., Gonin, M., Fuhrer, K., Kulmala, M.,
460 and Worsnop, D. R.: A high-resolution mass spectrometer to measure atmospheric ion composition, *Atmos Meas Tech*, 3, 1039–1053, https://doi.org/10.5194/amt-3-1039-2010, 2010.

Kammler, H. K., Jossen, R., Morrison, P. W., Pratsinis, S. E., and Beaucage, G.: The effect of external electric fields during
flame synthesis of titania, *Powder Technol*, 135–136, 310–320, https://doi.org/10.1016/j.powtec.2003.08.023, 2003.

465 Kim, S. K., Chang, H., Cho, K., Kil, D. S., Cho, S. W., Jang, H. D., Choi, J. W., and Choi, J.: Enhanced photocatalytic
property of nanoporous TiO₂/SiO₂ micro-particles prepared by aerosol assisted co-assembly of nanoparticles, *Mater Lett*, 65, 3330–3332, https://doi.org/10.1016/j.matlet.2011.02.028, 2011.

Larriba, C., Hogan, C. J., Attoui, M., Borrajo, R., Garcia, J. F., and De La Mora, J. F.: The mobility-volume relationship
below 3.0 nm examined by tandem mobility-mass measurement, *Aerosol Science and Technology*, 45, 453–467,
470 https://doi.org/10.1080/02786826.2010.546820, 2011.



Li, S., Ren, Y., Biswas, P., and Tse, S. D.: Flame aerosol synthesis of nanostructured materials and functional devices: Processing, modeling, and diagnostics, *Prog Energy Combust Sci*, 55, 1–59, <https://doi.org/10.1016/j.pecs.2016.04.002>, 2016.

Li, Y. H., Chen, C. T., and Fang, H. K.: Effects of a microwave-induced corona discharge plasma on premixed methane-air 475 flames, *Energy*, 188, 116007, <https://doi.org/10.1016/j.energy.2019.116007>, 2019.

Liao, Y. H. and Zhao, X. H.: Plasma-Assisted Stabilization of Lifted Non-premixed Jet Flames, *Energy and Fuels*, 32, 3967–3974, <https://doi.org/10.1021/acs.energyfuels.7b03940>, 2018.

Lovejoy, E. R., Curtius, J., and Froyd, K. D.: Atmospheric ion-induced nucleation of sulfuric acid and water, *Journal of Geophysical Research D: Atmospheres*, 109, D08204, <https://doi.org/10.1029/2003JD004460>, 2004.

480 Niu, F., Li, S., Zong, Y., and Yao, Q.: Catalytic behavior of flame-made Pd/TiO₂ nanoparticles in methane oxidation at low temperatures, *Journal of Physical Chemistry C*, 118, 19165–19171, <https://doi.org/10.1021/jp504859d>, 2014.

Ohisa, H., Kimura, I., and Horisawa, H.: Control of Soot Emission of a Turbulent Diffusion Flame by DC or AC Corona Discharges, *Combust Flame*, 116, 653–661, [https://doi.org/10.1016/S0010-2180\(98\)00054-6](https://doi.org/10.1016/S0010-2180(98)00054-6), 1999.

485 Pratsinis, S. E.: Flame aerosol synthesis of ceramic powders, *Prog Energy Combust Sci*, 24, 197–219, [https://doi.org/10.1016/S0360-1285\(97\)00028-2](https://doi.org/10.1016/S0360-1285(97)00028-2), 1998.

Ren, Y., Li, S., Zhang, Y., Tse, S. D., and Long, M. B.: Absorption-Ablation-Excitation Mechanism of Laser-Cluster Interactions in a Nanoaerosol System, *Phys Rev Lett*, 114, 093401, <https://doi.org/10.1103/PhysRevLett.114.093401>, 2015.

490 Ren, Y., Cui, W., and Li, S.: Electrohydrodynamic instability of premixed flames under manipulations of dc electric fields, *Phys Rev E*, 97, 013103, <https://doi.org/10.1103/PhysRevE.97.013103>, 2018.

Rosocha, L. A., Coates, D. M., Platts, D., and Stange, S.: Plasma-enhanced combustion of propane using a silent discharge, *Phys Plasmas*, 11, 2950–2956, <https://doi.org/10.1063/1.1688788>, 2004.

Saito, M., Arai, T., and Arai, M.: Control of Soot Emitted from Acetylene Diffusion Flames by Applying an Electric Field, *Combust Flame*, 119, 356–366, [https://doi.org/10.1016/S0010-2180\(99\)00065-6](https://doi.org/10.1016/S0010-2180(99)00065-6), 1999.

495 Schulz, F., Commodo, M., Kaiser, K., De Falco, G., Minutolo, P., Meyer, G., D'Anna, A., and Gross, L.: Insights into incipient soot formation by atomic force microscopy, *Proceedings of the Combustion Institute*, 37, 885–892, <https://doi.org/10.1016/j.proci.2018.06.100>, 2019.

Siefering, K. L. and Griffin, G. L.: Growth Kinetics of CVD TiO₂: Influence of Carrier Gas, *J Electrochem Soc*, 137, 1206–1208, <https://doi.org/10.1149/1.2086632>, 1990.

500 Spicer, P. T., Artelt, C., Sanders, S., and Pratsinis, S. E.: Flame synthesis of composite carbon black-fumed silica nanostructured particles, *J Aerosol Sci*, 29, 647–659, [https://doi.org/10.1016/S0021-8502\(97\)10023-4](https://doi.org/10.1016/S0021-8502(97)10023-4), 1998.

Su, H. C., Goyal, H., Clark, L., Kook, S., Hawkes, E., Chan, Q. N., Padala, S., Le, M. K., and Ikeda, Y.: In-Cylinder Soot Reduction Using Microwave Generated Plasma in an Optically Accessible Small-Bore Diesel Engine, *SAE Technical Papers*, 2018-01-0246, <https://doi.org/10.4271/2018-01-0246>, 2018.



505 Tang, Y., Simeni Simeni, M., Yao, Q., and Adamovich, I. V.: Non-premixed counterflow methane flames in DC/AC/NS electric fields, *Combust Flame*, 240, 112051, <https://doi.org/10.1016/j.combustflame.2022.112051>, 2022.

Thimsen, E., Rastgar, N., and Biswas, P.: Nanostructured TiO₂ films with controlled morphology synthesized in a single step process: Performance of dye-sensitized solar cells and photo watersplitting, *Journal of Physical Chemistry C*, 112, 4134–4140, <https://doi.org/10.1021/jp710422f>, 2008.

510 Ude, S. and De La Mora, J. F.: Molecular monodisperse mobility and mass standards from electrosprays of tetra-alkyl ammonium halides, *J Aerosol Sci*, 36, 1224–1237, <https://doi.org/10.1016/j.jaerosci.2005.02.009>, 2005.

Vemury, S. and Pratsinis, S. E.: Corona-assisted flame synthesis of ultrafine titania particles, *Appl Phys Lett*, 66, 3275–3277, <https://doi.org/10.1063/1.113402>, 1995.

Veronesi, S., Commodo, M., Basta, L., De Falco, G., Minutolo, P., Kateris, N., Wang, H., D'Anna, A., and Heun, S.: 515 Morphology and electronic properties of incipient soot by scanning tunneling microscopy and spectroscopy, *Combust Flame*, 243, 111980, <https://doi.org/10.1016/j.combustflame.2021.111980>, 2022.

Vincent-Randonnier, A., Larigalde, S., Magre, P., and Sabel'nikov, V.: Experimental study of a methane diffusion flame under dielectric barrier discharge assistance, *IEEE Transactions on Plasma Science*, 35, 223–232, <https://doi.org/10.1109/TPS.2007.893249>, 2007.

520 Vishnyakov, V. I., Kiro, S. A., and Ennan, A. A.: Heterogeneous ion-induced nucleation in thermal dusty plasmas, *J Phys D Appl Phys*, 44, 215201, <https://doi.org/10.1088/0022-3727/44/21/215201>, 2011.

Wang, Y., Liu, P., Fang, J., Wang, W. N., and Biswas, P.: Kinetics of sub-2 nm TiO₂ particle formation in an aerosol reactor during thermal decomposition of titanium tetraisopropoxide, *Journal of Nanoparticle Research*, 17, 147, <https://doi.org/10.1007/s11051-015-2964-y>, 2015.

525 Wang, Y., Kangasluoma, J., Attoui, M., Fang, J., Junninen, H., Kulmala, M., Petäjä, T., and Biswas, P.: Observation of incipient particle formation during flame synthesis by tandem differential mobility analysis-mass spectrometry (DMA-MS), *Proceedings of the Combustion Institute*, 36, 745–752, <https://doi.org/10.1016/j.proci.2016.07.005>, 2017a.

Wang, Y., Kangasluoma, J., Attoui, M., Fang, J., Junninen, H., Kulmala, M., Petäjä, T., and Biswas, P.: The high charge fraction of flame-generated particles in the size range below 3 nm measured by enhanced particle detectors, *Combust Flame*, 176, 72–80, <https://doi.org/10.1016/j.combustflame.2016.10.003>, 2017b.

530 Xiong, G., Kulkarni, A., Dong, Z., Li, S., and Tse, S. D.: Electric-field-assisted stagnation-swirl-flame synthesis of porous nanostructured titanium-dioxide films, *Proceedings of the Combustion Institute*, 36, 1065–1075, <https://doi.org/10.1016/j.proci.2016.08.079>, 2017.

Yang, Y., Chen, H., Li, C., and Wang, P.: Ion induced nucleation of charged droplets enhanced by external electric field, *Phys Plasmas*, 31, 073505, <https://doi.org/10.1063/5.0196881>, 2024.

Zhao, B., Yang, Z., Wang, J., Johnston, M. V., and Wang, H.: Analysis of soot nanoparticles in a laminar premixed ethylene flame by scanning mobility particle sizer, *Aerosol Science and Technology*, 37, 611–620, <https://doi.org/10.1080/02786820300908>, 2003.



540 Zhao, H., Liu, X., and Tse, S. D.: Control of nanoparticle size and agglomeration through electric-field- enhanced flame synthesis, *Journal of Nanoparticle Research*, 10, 907–923, <https://doi.org/10.1007/s11051-007-9330-7>, 2008.